

Surface Phase Diagrams from Nested Sampling

Mingrui Yang,[†] Livia B. Pártay,[‡] and Robert B. Wexler^{*,†}

[†]*Department of Chemistry and Institute of Materials Science and Engineering, Washington University in St. Louis, St. Louis, MO 63130, USA*

[‡]*Department of Chemistry, University of Warwick, Coventry, CV4 7AL, UK*

E-mail: wexler@wustl.edu

Abstract

Atomic-scale modeling of surface phase equilibria often focuses on temperatures near zero Kelvin due to the difficulty in computing the free energy of surfaces at finite temperatures. The Bayesian-inference-based nested sampling (NS) algorithm allows modeling surface phase equilibria at arbitrary temperatures by directly and efficiently calculating the partition function, whose relationship with free energy is well known. In this work, we extend NS to calculate surface phase diagrams, including all relevant translational, rotational, and vibrational contributions to the free energy. We apply NS to the surfaces of the Lennard-Jones solid, recording energies through the iterative compression of surface phase space rather than a specific cooling schedule. We construct the partition function from these recorded energies to calculate ensemble averages of thermodynamic properties, such as the constant-volume heat capacity and temperature-dependent order parameters that characterize the surface structure. Key results include determining the nature of phase transitions on flat and stepped surfaces, which typically feature an enthalpy-driven condensation at higher temperatures and an entropy-driven reordering process at lower temperatures, and the presence of critical points on the phase diagrams of most of the flatter facets. Overall, we demonstrate the ability and potential of NS for surface modeling and, ultimately, materials discovery.

1 Introduction

The structure and composition of solid surfaces play an essential role in determining their properties for various high-stakes applications, including gas sensing¹ and optoelectronics,² in addition to those central to mitigating the effects of climate change, such as photovoltaics³ and catalysis. For the latter, it has been shown that *in situ* surface reconstruction, *i.e.*, changes in the structure and composition of the topmost layers of a solid, can govern the activity and selectivity of heterogeneous catalysts for the CO₂ reduction,^{4,5} H₂ evolution,^{6–8} O₂ evolution,^{9–11} and O₂ reduction reactions,¹² to name a few examples. Therefore, designing catalysts for these reactions and functional materials for other surface-specific processes requires an atomic-scale understanding of surface reconstruction and its dependence on operating conditions. However, the experiments that can measure these properties are typically done under conditions that differ from operating conditions,¹³ with only a few exceptions.¹⁴

To fill this need for, ideally, atomic-scale information about *in situ* surface phases, the field has often turned to computer simulations, which typically fall under one of three categories: thermodynamic, optimization-based, and statistical thermodynamic approaches. The most notable example of the former is *ab initio* surface thermodynamics, pioneered by Reuter and Scheffler.¹⁵ In this approach, one uses quantum-mechanics-based simulation techniques to calculate the surface grand potentials for a set of slabs (see Figure 1 for an example of a surface slab model), whose structures and compositions typically are guided by chemical intuition. The resulting surface grand potentials usually are approximate because only those finite-temperature effects associated with the enthalpy and entropy of harmonic vibrations are included, if at all. The contributions due to anharmonic vibrations, rotations, and configurational degrees of freedom are commonly ignored¹⁶ to make surface calculations computationally tractable, especially when employing an *ab-initio*-based description of the chemical bonds, such as density functional theory.

While *ab initio* thermodynamics can be insightful, in the absence of experimental input, the variety of possible surface structures one must intuit is wide. Enter the optimization-

based approaches, which have shown promise in navigating the complexity of surface phase space more systematically. These include enumerating mean-field configurations,¹⁷ random structure searching,¹⁸ simulated annealing,¹⁹ basin hopping,²⁰ global activity search,²¹ stochastic surface walking,²² evolutionary/genetic algorithms,^{23–26} particle swarm optimization,²⁷ active learning,²⁸ and reinforcement learning.²⁹ The methods above guide the search for structures that minimize the surface energy or enthalpy as a function of composition at zero Kelvin, which are used as inputs for *ab initio* thermodynamics. Lately, several groups have used Monte Carlo (MC) simulations in the canonical,³⁰ grand canonical,^{31–34} and semi-grand canonical ensembles³⁵ to aid the discovery of *in situ* surface phases, where the constant thermodynamic state variables can be tunable. However, these approaches commonly omit a complete treatment of entropy since they do not provide the capability to compute the partition function and hence the absolute free energy. Therefore, they cannot be expected to produce accurate surface phase diagrams unless entropic contributions are known to be negligible.

Recently, Zhou, Scheffler, and Ghiringhelli introduced an approach to efficiently estimate the free energy of surfaces from replica-exchange grand-canonical sampling and the multi-state Bennett acceptance ratio method.¹⁶ While their algorithm was a significant advance by accounting for anharmonic contributions to the free energy, the need, however, for regular temperature and chemical potential grids in replica-exchange simulations can coarsen phase space sampling at surface phase transitions. We propose an alternative approach based on nested sampling (NS), which avoids such coarsening by constructing a set of slabs equidistant in surface phase space volume. NS was first introduced in Bayesian statistics,^{36,37} and was later adopted by various research fields³⁸ and adapted to sample the potential energy surface (PES) of atomic-scale systems.^{39–41} The power of NS has been demonstrated in studying various systems, including the formation of clusters,^{42,43} calculation of the quantum partition function,⁴⁴ sampling transitions paths,⁴⁵ as well as the calculation of the pressure-temperature phase diagram for various metals, alloys, and model potentials,^{46–49} which often

identified previously unknown stable solid phases.

This study uses NS to calculate coverage-temperature surface phase diagrams as a proof-of-concept for future investigations of more complex materials interfaces and interfacial conditions. We carry out NS for surfaces of the Lennard-Jones (LJ) solid by constructing the partition function from energy values gathered during a process that compresses the surface phase space volume by a constant factor at each iteration. Utilizing the constructed partition function, we compute ensemble averages of thermodynamic properties such as the constant-volume heat capacity and order parameters that describe the surface structure. Notably, we identify phase transitions both on flat and stepped surfaces. Most flat surfaces exhibit an enthalpy-driven condensation at higher temperatures, an entropy-driven reordering process within the condensed layer at lower temperatures, and a critical coverage above which a disordered adsorbate phase is unstable. Ultimately, we showcase the capabilities and potential of NS for surface modeling and materials discovery.

2 Computational Methods

2.1 Nested Sampling

2.1.1 Algorithm

NS is an approach to calculating Bayesian evidence, which, in statistical mechanics, corresponds to the partition function. In NS, the sampling is performed by independent configurations, usually called “walkers” or “live points.” It is started by drawing a set of atomic configurations from a uniform prior distribution in configurational space, *i.e.*, a set of random, high-energy, ideal-gas-like configurations. These configurations define a set of likelihood values whose negative natural logarithms are analogous to the total energies of the configurations. During each step of the iterative process of NS, the configuration with the highest energy (*i.e.*, the smallest likelihood value) is identified, its contribution to the

canonical partition function (*i.e.*, the evidence) is calculated, and then this walker is discarded. Then, a new configuration is drawn from the set of random configurations (*i.e.*, the prior distribution) but with a constraint: its total energy (*i.e.*, the negative natural logarithm of its likelihood value) must be less than (*i.e.*, greater than, for the likelihood value) that of the discarded configuration. This process is repeated until the lowest energy structure is identified. The idea is that the distribution of configurations is “narrowed down” or “nested” into regions of decreasing total energy. This approach provides a very efficient way of exploring configurational spaces where most low-total-energy configurations are located within a small fraction of the phase space volume, a common occurrence in systems that follow the Boltzmann distribution.

Previous works have described the algorithm in detail for applications for clusters at constant volume^{39,50} and bulk materials at constant pressure,^{40,41} here we will concentrate on the surface-specific description. In the case of NS for surfaces, we distinguish particles constituting the surface and those that adsorb or condense onto the surface. While these free-moving particles are positioned randomly, the surface particles have a fixed structure that remains unchanged during the sampling. To distinguish the two classes of particles, we will refer to the *free particles* whenever the coordinates were allowed to change (even at stages where these particles are condensed onto the surface) and to *surface particles* for those constituting the fixed slab of particles. While the approximation of fixed surface particles requires further exploration, our preliminary findings suggest it does not significantly impact our results. As shown in Figure S1 in the Supporting Information, adding multiple monolayers (MLs) of free particles does not qualitatively alter (*e.g.*, change the number of coexistence curves in) the surface phase diagram of LJ(111) with a 2×2 surface unit cell. Therefore, we anticipate that introducing further complexities, such as surface particle vibrations, will likely serve to fine-tune, rather than drastically change, our sampling of the relevant phase space volume, except for metastable or soft materials. The number of walkers, K , remains constant during the sampling and determines the sampling resolution.

Once the initial configurations, the walkers, are generated, the iterative part of the sampling is commenced as follows:

1. From the set of walkers, pick and record the configuration with the highest total energy, $E_i^{\max} = \max\{E\}$. The phase space volume, Γ , of the PES below E_i^{\max} is $\Gamma_i = [K/(K+1)]^i$.
2. Replace the highest total energy walker with a new configuration, which is chosen randomly but such that $E^{\text{new}} < E_i^{\max}$. Due to the drastic shrinking of the available phase space volume as lower total energy levels are sampled, the probability of generating an acceptable random configuration diminishes. Hence, we generated new configurations by cloning an existing walker and performing a walk, either through MC or total energy Hamiltonian MC,^{40,41} such that the PES has been explored and the configuration is decorrelated from its starting point.
3. Let $i \leftarrow i + 1$ and return to Step 1.

Once sufficiently low-total-energy regions of configurational space are explored, the sampling can stop, and, using the series of saved total energy values for the replaced walkers, we can calculate the partition function, Z , as

$$Z(N, V, \beta) = \sum_i w_i \exp[-\beta E_i(N, V)], \quad (1)$$

where N is the number of particles, V is the volume, $\beta = 1/(k_B T)$ is the thermodynamic temperature, and w_i is the NS weight of the i -th iteration, $w_i = \Gamma_i - \Gamma_{i+1}$. Since this iterative sampling procedure (see Steps 1-3 above) is temperature independent (temperature is only considered in post-processing steps), one can substitute any β into Equation 1 and therefore calculate the partition function at any temperature. Due to the “top-down” nature of the algorithm, NS does not require prior knowledge of structural or thermodynamic properties, making it an ideal tool for an unbiased and exhaustive exploration of the PES,

particularly suited to identify phase transitions and thermodynamically relevant phases. We should finally note that considering the potential energy contribution of the fixed particles constituting the surface will affect the absolute value of the partition function. However, we are interested in thermodynamic response functions that are a derivative of Z , such as the heat capacity, and hence insensitive to the energy scale. Nevertheless, one should make an informed decision about the surface contribution in specific cases. Furthermore, since we keep the surface particles fixed, our calculations only consider the kinetic contribution of the free particles.

2.1.2 Phase Equilibria

For a first-order phase transition at constant volume, the system's constant-volume heat capacity, C_V , tends to diverge in the limit of an infinitely large system (although for finite systems, it just becomes a large peak). Therefore, we can use peaks in C_V to locate first-order phase transition coverages and temperatures. We calculate C_V as a function of β , whose relationship with Z is well known, *i.e.*,

$$C_V(\beta) = k_B \beta^2 \left(\frac{\partial^2 \ln Z}{\partial \beta^2} \right)_{N,V}. \quad (2)$$

We then locate peaks on the $C_V(\beta)$ curve for different coverages and manually connect adjacent peaks for neighboring coverages to construct a coverage-temperature phase diagram.

With access to the canonical partition function, we can also calculate the ensemble average of any configuration-dependent property, $A(\mathbf{r}_i)$, at a given temperature, β , as

$$\langle A(\beta) \rangle = \frac{\sum_i A(\mathbf{r}_i) w_i \exp(-\beta E_i)}{Z(\beta)}. \quad (3)$$

To gain insight into the phase-transition-induced changes in the structure of LJ surfaces, we calculate surface order parameters, such as the average vertical position of the free particles, $\langle \Delta z \rangle$, relative to that of the fixed surface particles, and the average coordination number,

$\langle \text{CN} \rangle$, of the free particles, including free-free and free-fixed particle-particle bonds, using Equation 3.

Furthermore, to identify a representative equilibrium structure of the system at some temperature β , we can calculate the probability, P , of sampling each structure from the canonical ensemble using

$$P_i(\mathbf{r}_i, \beta) = \frac{w_i \exp[-\beta E(\mathbf{r}_i)]}{Z(\beta)}. \quad (4)$$

where we write E_i as $E(\mathbf{r}_i)$ to highlight the fact that the structure \mathbf{r} of state i determines its potential energy E . The structure that maximizes P_i at some temperature β is the one that is most likely to occur at that temperature.

2.2 Simulation Details

2.2.1 Lennard-Jones Potential

In this study, we use the well-explored LJ potential to test the effectiveness of NS for predicting surface phase diagrams. The LJ potential provides a simple but physical model for surfaces interacting through spherically symmetric van der Waals-type forces. The LJ potential is typically expressed as

$$V_{\text{LJ}}(r) = 4\epsilon \left[\left(\frac{\sigma}{r}\right)^{12} - \left(\frac{\sigma}{r}\right)^6 \right], \quad (5)$$

where ϵ and σ serve as units for energy and distance, respectively. We use the same σ for the free and fixed particles and the same ϵ for free-free, free-fixed, and fixed-fixed particle interactions to model a pure LJ solid. We shifted the LJ potential to ensure the energy was zero at the cutoff radius of 4σ .

2.2.2 Surface System Setup

To sample the phase space of free LJ particles above a fixed LJ surface, we divide the simulation cell into three regions from bottom to top (see Figure 1 for an example of the setup):

- **Region 1:** A slab with fixed particles and a thickness of $\approx 4\sigma$, depending on the surface features, *e.g.*, flat or stepped. The slab contains several layers with the same number of particles and a fixed interlayer spacing that depends on the surface features (see Table S1 in the SI for a more detailed description of different slabs). We define the surface coverage, θ , as the number of free particles divided by the number of fixed particles in a single layer.
- **Region 2:** A space that extends 4σ above the fixed slab, where the free particles can interact with the fixed slab and each other. The initial walkers randomly and uniformly sample this region. We limit the space to a thickness of $\leq 4\sigma$ (*i.e.*, the value of the LJ cutoff radius) to exclude any space where the free particles do not interact with the slab (we call these “voids”). Currently, `pymatnest` updates the MC step size to maintain an acceptance ratio of ≈ 0.3 . However, MC steps do not change the potential energy when particles enter these voids, which decreases the acceptance ratio (because we accept the MC step only if the potential energy remains below E_i^{\max}) and, consequently, the MC step size to restore an acceptance ratio of ≈ 0.3 . We will address this limitation in a future code release.
- **Region 3:** The topmost region is an impenetrable vacuum, enforced by a reflective wall 4σ below the top of the cell that prevents the free particles from interacting with the bottom of the slab (an artifact) due to periodic boundary conditions.

For systems having only one or two free particles or a disproportionately large gas phase region where the particles fall outside the interaction range of the surface, the sampling

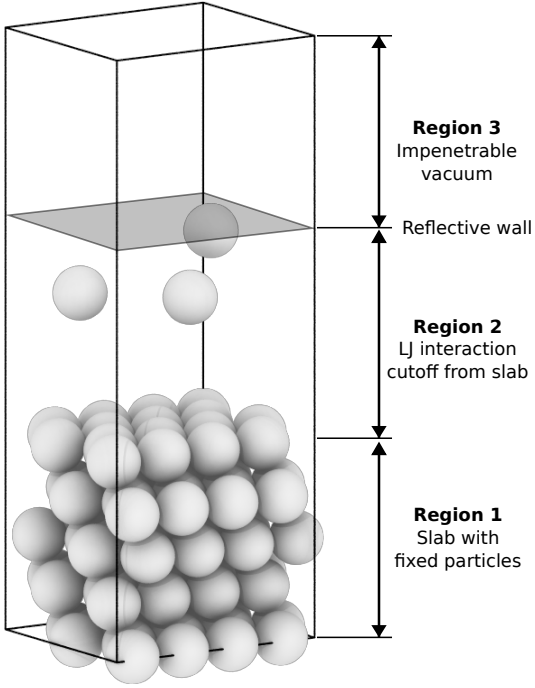


Figure 1: An example of the surface system setup, showing a five-layer LJ(111) slab with a 4×4 surface unit cell (16 fixed particles per layer) and three free particles, corresponding to a maximum possible coverage of $\theta = 3/16$ ML. From bottom to top, the three regions are as follows: (1) a slab with fixed particles and a thickness of $\approx 4\sigma$; (2) a sampled region where free particles can interact with the slab and other free particles; and (3) an $\approx 4\sigma$ -thick impenetrable vacuum to prevent the free particles from interacting with the periodic image of the bottom of the slab.

can struggle to find the condensation transition. In this case, additional measures could be necessary to ensure that NS proceeds to subsequent iterations by avoiding regions of configurational space where neighboring configurations have the same potential energy due to being outside the range of interaction with the surface. We describe such scenarios and solutions in the SI.

2.2.3 Nested Sampling Parameters

We used 80 walkers per free particle for the NS calculations of surfaces. The required number of NS iterations scales quasi-linearly with the number of walkers; we set it to be 250 iterations per walker, as our tests showed this number was large enough for all surfaces to

reach their ground-state structures. This scaling means that for the highest coverage runs, we performed 320,000 NS iterations. During each NS iteration, we replaced only the single highest potential energy walker with a new configuration that we generated by cloning an existing walker and decorrelating it from its cloned configuration with MC translational moves. In Figure 2, we illustrate a common trend in how the highest energy varies during an NS run. At the start, the algorithm quickly identifies and replaces the high-energy states with minimal contributions to the partition function due to their small Boltzmann factors. Such high-energy states often arise from the proximity of two or more particles, leading to increased energy due to the LJ repulsion. Following this, the energies sampled gradually decrease, converging toward the system’s ground-state energy. We automatically adjusted the MC-translational-move step size by gradually reducing it as the sampling progressed to control the new configuration acceptance rate. We kept the simulation cell shape and volume constant during the sampling. We saved the replaced configurations every 100 NS iterations, later using these structures to compute the surface order parameters and examine some metastable states. Finally, we performed three independent NS calculations for each system, with identical NS parameters but unique sets of initial walkers. The initial configurations were generated by depositing particles in **Region 2** of Figure 1 at coordinates drawn from a random uniform distribution. Additionally, we found that the structures sampled in independent NS calculations but at the same temperature range are consistent. We have implemented surface NS in the open-source `pymatnest` code, freely available at <https://libatoms.github.io/pymatnest>.

3 Results

We used surface NS to predict the phase diagrams for four facets of the face-centered-cubic (fcc) LJ solid. We considered two flat facets, (111) and (100), and two stepped facets, (311) and (110), to analyze the effect of planarity on surface phase equilibria. Additionally, we

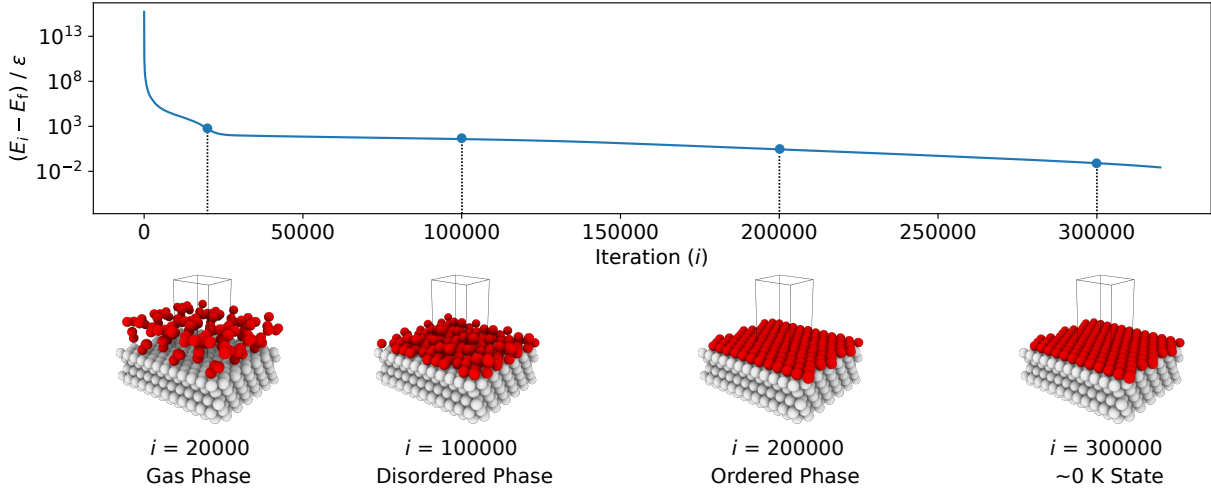


Figure 2: The recorded energies, E_i relative to the final energy (*i.e.*, the ground-state energy near zero Kelvin), E_f , versus the number of iterations, i , from an NS calculation, using 1,280 walkers at full coverage. The energy decreases rapidly during the initial sampling stage (first 30,000 iterations), as the phase space shrinks quickly when the walkers explore the high-energy region of the PES. Then the energy decreases slower, capturing different configurations with almost degenerate energies. Snapshots of the system illustrate the phase changes from an initial ideal-gas-like phase to a condensed but disordered phase, then to an ordered state. Fixed particles are shown in grey and free particles in red.

chose these four specific facets because they are some of the lowest index, lowest surface energy, and highest surface area fraction facets on the Wulff shape of fcc elemental solids,⁵¹ thus imbuing our predicted surface phase diagrams with added practical relevance. We focus on the flat LJ(111) and stepped LJ(311) surfaces, given the similarities in the calculated coverage- and temperature-dependent properties of LJ(111) and LJ(100), as well as those of LJ(110) and LJ(311). The Support Information includes and discusses the LJ(100) and LJ(110) results. We constructed slabs with a 4×4 surface unit cell and the following numbers of layers: five for LJ(111), eight for LJ(110), six for LJ(100), and eight for LJ(311). Different facets require different numbers of layers due to their different interlayer spacing (see Table S1 in the SI). We used these numbers of layers to ensure that the bottom surface is the deepest possible layer within the LJ cutoff radius from free particles adsorbed on the surface, representing a semi-infinite bulk crystal beneath the top surface. For each facet, the number of free particles included in the NS calculations ranges from one to 16. With 16 free

particles, a monolayer (ML) can be formed on the fixed slab.

3.1 Flat LJ(111) Surface

Following the procedure described in Section 2, we first compute $C_V(T^*)$ for the flat LJ(111) surface with coverages ranging from $\theta = 1/16$ ML to one ML (*i.e.*, $\theta = 16/16$ ML). C_V curves for the LJ(111) surface (see Figure 3a) display different behaviors in the lower coverage ($\theta < 12/16$ ML) and higher coverage ($\theta \geq 12/16$ ML) regimes. In the case of the lower coverage surfaces, two peaks in the C_V curve can be observed. From higher to lower temperatures, a broad and shallow peak in C_V occurs between $0.5 - 1.0 k_B T/\epsilon$ and has a very weak coverage dependence. At $T < 0.5 k_B T/\epsilon$, a sharper peak appears, exhibiting a stronger coverage dependence. At coverages above $\theta \geq 12/16$ ML, the two C_V peaks merge, rising sharply as the coverage increases toward one ML.

To determine the peak positions and hence the surface phase transition temperatures, we used the `scipy.signal.find_peaks()` function with `prominence=0.02` to automatically find peaks for each C_V curve. The resulting coverage-temperature phase diagram for the LJ(111) surface (see Figure 3b, where each “ \times ” marks a peak found by the automatic peak finder) shows two distinct surface phase boundaries for coverages lower than $13/16$ ML, as expected. A triple-point appears at $\theta = 13/16$ ML and $\approx 0.63 k_B T/\epsilon$.

To characterize the surface phases and their transitions, we calculated two order parameters, $\langle \Delta z \rangle$ (see Figure 3c) and $\langle CN \rangle$ (see Figure 3d), as described in Section 2. As expected, $\langle \Delta z \rangle$ decreases as the temperature decreases because the free particles start adsorbing on the surface; we will refer to this process as surface condensation. The 1.2σ contour coincides with the higher temperature coexistence curve, suggesting that the adsorbed free particles form a quasi-two-dimensional layer with a thickness equal to $\approx 1.2\sigma$ upon cooling. Note that 0.92σ is the interlayer spacing in an LJ(111) bulk, meaning, on average, the free particles are now near the positions where an additional monolayer should form. Since the higher temperature surface phase transition corresponds to a vertical ordering of the free parti-

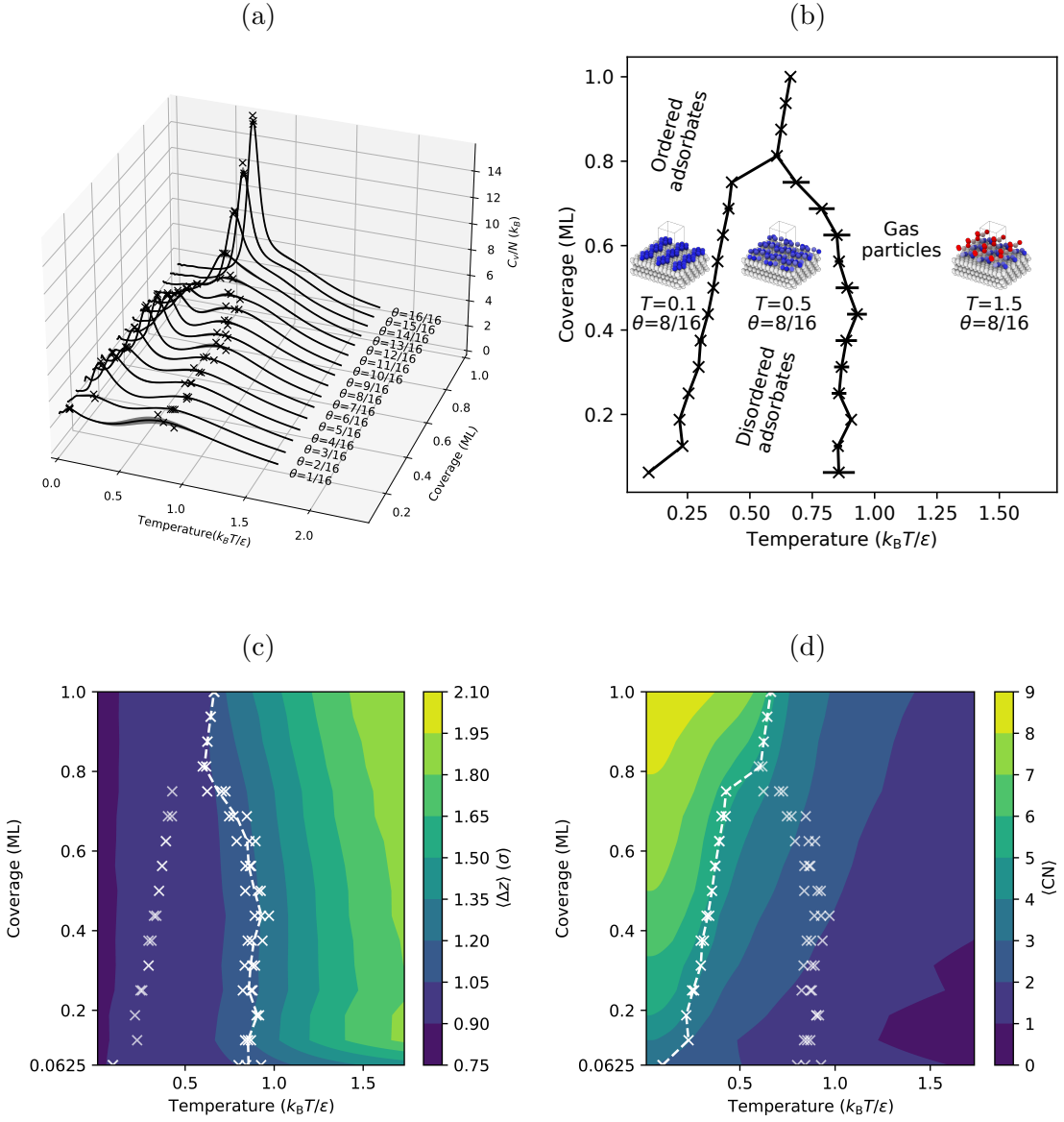


Figure 3: Calculated coverage-temperature properties of the flat LJ(111) surface with fractional coverages from $\theta = 1/16$ ML up to one ML: (a) heat capacity per free particle, with the peaks on the curves marked with crosses (\times), (b) phase diagram with insets showing the maximum-probability structures from each phase at selected temperatures for $\theta = 8/16$ ML, (c) average z -coordinates of the free particles relative to the topmost layer in the fixed slab, note that in an LJ(111) bulk the interlayer spacing is 0.92σ , and (d) average coordination numbers of the free particles including both particle-particle and particle-surface bonding. The error bars in panel (b) are the standard deviations of the peak temperatures for the three independent NS runs at each coverage. The lines between the crosses in panels (b)-(d) are only guides for the eye.

cles, the lower temperature surface phase transition must correspond to the approximately two-dimensional ordering of the free particles (or adsorbates, after condensation) within the surface layer. Thus, we can see that, although very close to the surface, these adsorbed particles will undergo a further ordering process. To quantify this surface-layer ordering, we calculated $\langle \text{CN} \rangle$, which increases with decreasing temperature (see Figure 3d). When the temperature is high, and the coverage is low, the free particles rarely interact with one another, resulting in a $\langle \text{CN} \rangle \approx 0$. However, once the temperature is less than that of the condensation, $\langle \text{CN} \rangle$ quickly reaches its maximum possible value: three for one free particle (because the free particle occupies a hollow site between three fixed surface particles), four for two free particles (because the two free particles occupy neighboring hollow sites), and so on. The maximum $\langle \text{CN} \rangle$ is nine, where an adsorbed free particle is closed-packed by six adsorbed free particles at neighboring hollow sites. Overall, the lower temperature coexistence curve coincides with a contour in $\langle \text{CN} \rangle$, separating a lower coordination surface phase with disordered adsorbates above the transition temperature from a higher coordination surface phase with ordered adsorbates below the transition temperature.

Interestingly, the LJ(111) surface has a triple point near a coverage of three-quarters ($\theta = 13/16$ ML) and at a temperature between the two surface phase transitions observed for lower coverages. For coverages $\theta \geq 13/16$, the C_V curves in Figure 3a show only one sharp peak. Since C_V is related to fluctuations in the total energy, such a sharp peak in C_V indicates a transition between surface phases with very different internal energies. Given the lack of a lower coordination surface phase with disordered adsorbates at intermediate temperatures for coverages $\theta \geq 13/16$ ML, we will refer to this process as surface deposition, where gas-phase free particles form a surface phase with ordered adsorbates below the deposition temperature. One can see from Figure 3c that the phase boundary now coincides with the $\langle \Delta z \rangle = 1.05\sigma$ contour versus the $\langle \Delta z \rangle = 1.20\sigma$ contour for the lower-coverage higher-temperature transition, showing that the phase transition processes happen closer to the fixed slab compared to the surface condensation. We can rationalize the origin of these

two different behaviors for lower and higher coverages – *i.e.*, condensation and deposition, respectively – by comparing the stable surface structures below the condensation and deposition temperatures, respectively (see Section S5 in the SI). For lower coverages, the free particles form islands and stripes (see the inset in Figure 3b for an example structure at $\theta = 8/16$ ML and $T = 0.1 k_{\text{B}}T/\epsilon$) on the surface with many isoenergetic options for reconfiguration. However, for higher coverages, the free particles form a continuous ML with vacancies, which have limited options for reconfiguration.

Another observation from our NS results is that, on the LJ(111) surface, the adsorbed free particles form a hexagonal-close-packed (hcp) ML on top of the fcc LJ solid at absolute zero. As it has been shown previously,⁵² the ground state stacking structure of the LJ solid depends on the treatment of the potential around the truncation distance, and in our specific setup, the total energy of the hcp ML is less than that of the fcc ML by $2 \times 10^{-7} \epsilon$ per adsorbed free particle. Thus, NS finds the hcp ML as the ground-state structure. On the other hand, molecular dynamics simulations show that forming an fcc ML on the fcc LJ(111) surface is kinetically favored.⁵³ However, Somasi et al. used an LJ cutoff radius of 2.5σ ; therefore, based on ref.⁵² we cannot simply compare their system to ours.

3.2 Stepped LJ(110) Surface

We next compute $C_V(T^*)$ for the stepped LJ(110) surface with the same coverages as those for the flat LJ(111) surface. We refer to the LJ(110) surface as stepped because it has “troughs” along one of the lateral directions. The C_V curves in Figure 4a show a dominant and almost coverage-independent peak (using the same automated procedure as that used in Section 3.1) at temperatures between $0.7 k_{\text{B}}T/\epsilon$ and $0.9 k_{\text{B}}T/\epsilon$ (see \times s). Note that a side peak can be observed at certain lower coverages (*e.g.*, $\theta = 3/16$ ML and $\theta = 4/16$ ML), but no clear trend emerges. The dominant and almost coverage-independent peak corresponds to a surface phase transition with a coverage-averaged phase transition temperature, \bar{T}_θ , of $0.80(3) k_{\text{B}}T/\epsilon$, as indicated by the dashed line in Figure 4a.

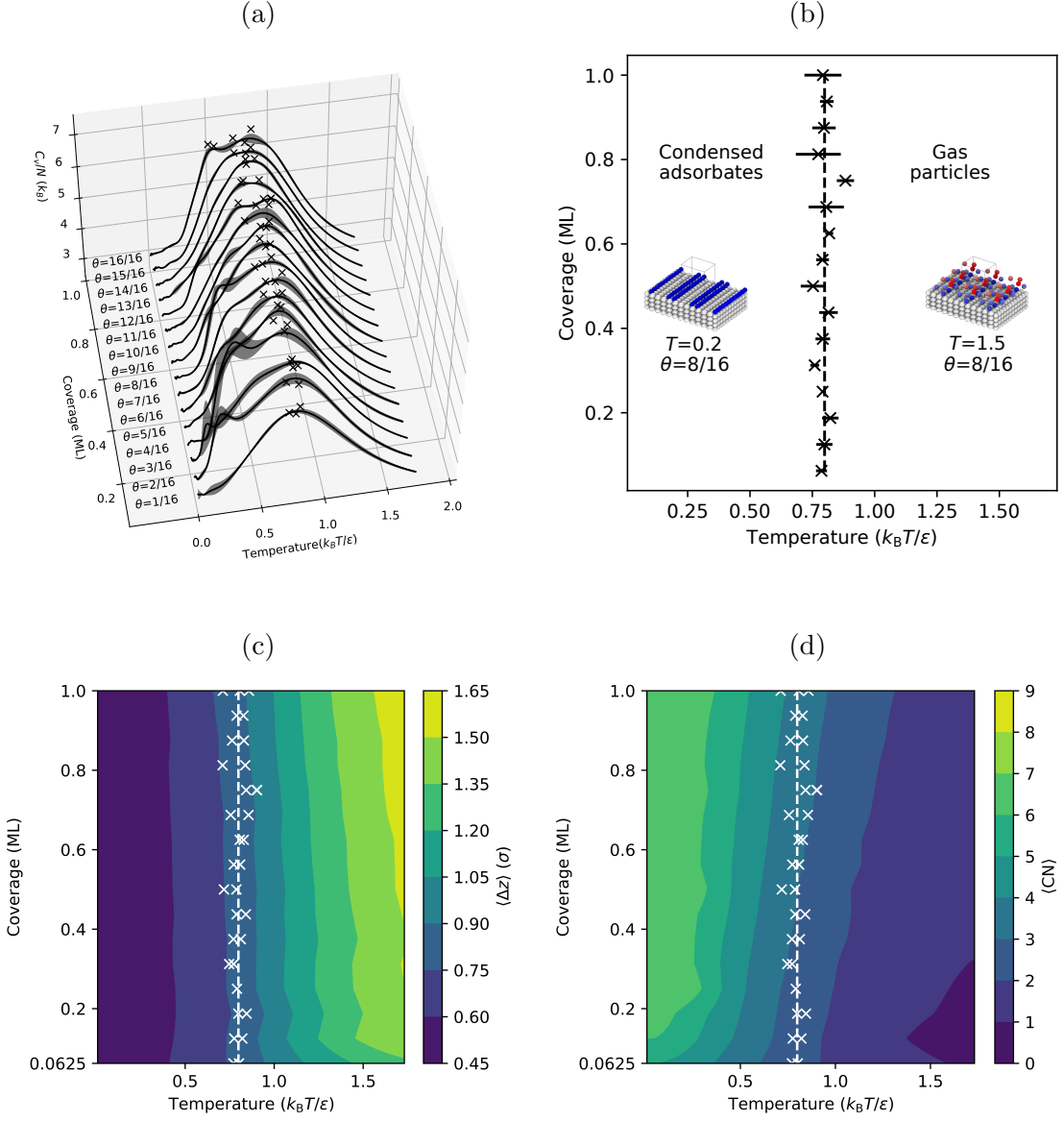


Figure 4: Calculated coverage-temperature properties of the flat LJ(110) surface with fractional coverages from $\theta = 1/16$ ML up to one ML: (a) heat capacity per free particle, with the peaks on the curves marked with crosses (\times), (b) phase diagram with insets showing the maximum-probability structures of each phase at selected temperatures for $\theta = 8/16$ ML, (c) average z -coordinates of the free particles relative to the topmost layer in the fixed slab, note that in an LJ(110) bulk the interlayer spacing is 0.56σ , and (d) average coordination numbers of the free particles including both particle-particle and particle-surface bonding. The dashed line at $\bar{T}_\theta = 0.80 k_B T/\epsilon$ shows the coverage-averaged phase transition temperature.

We calculated $\langle \Delta z \rangle$ to characterize the surface phases and their transitions. Figure 4c shows that, at the highest temperature considered (*i.e.*, $T \approx 1.73 k_B T/\epsilon$), $\langle \Delta z \rangle = 1.65\sigma$ is nearly equal to the vertical center of **Region 2** in the simulation cell, *i.e.*, 1.72σ (See Table S1 in the SI). At \bar{T}_θ , $0.75\sigma < \langle \Delta z \rangle < 0.90\sigma$. Note that in a perfect LJ(110) bulk, the $\Delta z_{\text{bulk}} = 0.84\sigma$ (the average of the trough site at 0.56σ and the atop site at 1.12σ). This matching between $\langle \Delta z \rangle$ and Δz_{bulk} suggests that the free particles “condense” on the stepped LJ(110) about one interlayer spacing above the surface, which was also observed on the LJ(111) in the previous section.

However, the nature of surface condensation on LJ(110) differs from that on LJ(111), as seen from the widths of their C_V peaks. To further characterize surface condensation, we calculate $\langle \text{CN} \rangle$ (see Figure 4d), which is approximately three at \bar{T}_θ . The average is derived from two scenarios: two free-fixed bonds when an adsorbed particle touches only one side of the trough and four when the particle touches both sides but has not fully settled into position. The coordination is at least fivefold when the particles are completely situated within the trough sites because they bind the fixed surface particles from two distinct layers, forming a square pyramidal structure. At absolute zero, $\langle \text{CN} \rangle$ is five for $\theta = 1/16$ ML (*i.e.*, five free-fixed bonds), six for $\theta = 2/16$ ML (*i.e.*, one free-free and five free-fixed bonds), and seven for $\theta \geq 3/16$ ML (*i.e.*, two free-free and five free-fixed bonds). Figure 4d also indicates that the free particles prefer to occupy the same trough if it has at least one unoccupied site because the maximum $\langle \text{CN} \rangle$ for $\theta \geq 3/16$ ML is seven, which is not possible if the free particles occupy different troughs.

In order to gain more insights into the phase transition, we calculate the ensemble average of the number of occupied troughs as a function of temperature at each coverage, as shown in Figure 5. From high to low temperature, we can see that in Figure 5 the occupancy of the troughs starts to increase as the free particles start to populate the troughs until the temperature reaches \bar{T}_θ for all coverages. When $T < \bar{T}_\theta$, for coverages $\theta > 12/16$ ML, the number of occupied troughs monotonically increases towards four. For coverages $\theta \leq 12/16$

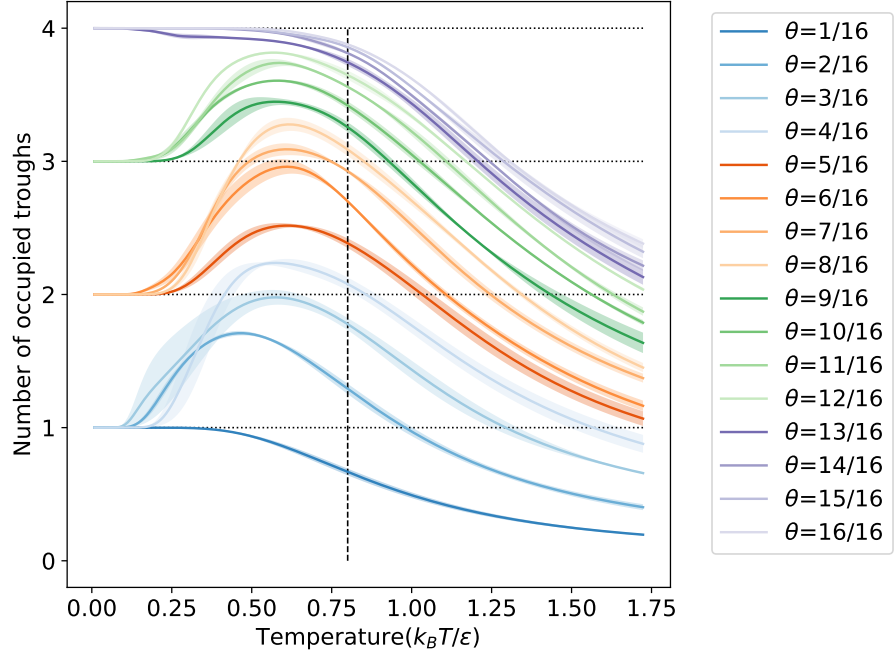


Figure 5: Ensemble-average number of occupied troughs as a function of temperature at each coverage. The shaded area around each curve indicates the standard deviation in the number of occupied troughs for the three independent NS runs. The horizontal dotted lines show the integer number of troughs. The vertical dashed line indicates the phase transition temperature $\bar{T}_\theta = 0.8 k_B T/\epsilon$.

ML, the number of occupied troughs decreases towards $\lceil N/4 \rceil$. Recall that four troughs exist in our unit cell, and each trough can accommodate four particles when forming a monolayer. Figure 5 shows that, when the temperature becomes lower than \bar{T}_θ , the free particles rapidly rearrange themselves into the same troughs when possible. A reduction in entropy typically accompanies the rearrangements, as the same-trough state is more ordered than the different-trough configuration, especially at the low coverage cases with many unoccupied binding sites. We believe that the rearrangement process is connected to the occurrence of the shoulder peaks on the C_V curves in Figure 4a at certain coverages. While it is difficult to establish a one-to-one correlation between this order parameter and peaks on the C_V curves, our order parameter suggests that an ordering phase transition occurs at temperatures close to the condensation transition.

In contrast to the flat LJ(111) surface, the stepped LJ(110) surface has higher coor-

dination binding sites in the troughs and hence offers stronger interactions with the free particles. Moreover, troughs reduce the number of isoenergetic adsorption sites, reducing the configurational entropy of the adsorbed free particles compared to LJ(111), for which adsorption at all hollow sites is effectively isoenergetic. This reduction leads to the near disappearance of an entropy-stabilized disordered adsorbates phase for the LJ(110) surface, as shown in Figure 4a. However, our results show that the LJ(110) surface undergoes a phase transition involving the trough-by-trough condensation of the gas-phase free particles as ordered adsorbates but only at certain coverages.

4 Discussion

First, we comment on the disappearance of the disordered adsorbate phase as one goes from more to less planar surfaces. Both of the planar surfaces we considered, i.e., (111) in Figure 3 of the main text and (100) in Figure S5 of the Supporting Information, adopt disordered adsorbate phases at intermediate temperatures. At the other end of the planarity spectrum, the stepped (110) surface does not have a stable disordered adsorbates phase (for reasons mentioned in Section 3.2). It goes directly from gas particles to ordered adsorbates during condensation. If one quantifies planarity as the depths of the troughs on the surface, then the troughs on the (311) surface are shallower than the ones on the stepped (110) surface (depth = 0.48σ vs. 0.56σ). Still, the (311) surface is (see SI), obviously, rougher than any of the planar surfaces (*i.e.* (111) and (100)). This intermediate planarity of the (311) surface manifests in its phase diagram as a smaller range of temperatures and coverages where the disordered adsorbates phase is stable (see Figure S6). In this way, the phase diagram of the (311) surface is also somewhere in between those of the planar and stepped surfaces, thus highlighting that planarity plays a leading role in determining the equilibrium geometry of adsorbates on LJ solids, which could have significant consequences for understanding the surfaces of metal and noble-gas elements.

We will now discuss the transferability of surface NS to other systems and conditions. This work shows that NS can compute the coverage-temperature phase diagrams of solid surfaces. However, other state variables, such as pressure and chemical potential, can be considered. For example, NS could be performed with particle addition and removal steps and translational moves to construct composition-temperature phase diagrams in the case of semi-grand canonical NS⁵⁴ and chemical potential-temperature phase diagrams in the case of grand canonical NS. Developing the latter will be an essential step toward the robust prediction of *in situ* surface reconstructions under operating conditions, which set the chemical potentials. Our implementation of NS also is not limited to the study of surface-adsorbate phase equilibria. Recall that we define a general interfacial system with two interacting subsystems: (1) a fixed *host* phase, which, in our case, is a surface slab model (see Figure 1) and (2) a free *guest* phase, which, in our case, are particles that begin as a randomly and uniformly distributed gas and end as an adsorbed ML. The generalization of this setup to other interfacial systems involves swapping out the *host* and *guest* with one's subsystems of interest. For example, consider the solid surface-liquid solvent interface in heterogeneous catalysis and typical rechargeable batteries. Here, the *host* would be the solid catalyst or electrode surface, and the *guest* would be the liquid, where the latter could be treated using explicit solvent particles coupled with implicit solvation in a continuous dielectric medium to improve computational efficiency. Alternatively, our approach could be extended to study the interfaces between two solids, such as those at grain boundaries (where reconstructions called complexions can form) and electrical junctions. In these cases, the *host* and *guest* would both be solids, but care would have to be taken in the selection or design of sampling moves to increase the acceptance ratio as it can be small in condensed phases.

Finally, to reiterate, we have adopted a simplified view of the surface, *i.e.*, as a *host* whose constituent particles can interact with other particles but cannot move for computational convenience. This simplification, however, precludes the surface from contributing to the free energy via its vibrational and configurational degrees of freedom. To include at least

some of these contributions, we propose the introduction of “flexible” surface particles that are neither fixed nor free but confined harmonically to their lattice sites. Such an approach, which we intend to develop in future work, would allow NS to capture the effect of harmonic surface vibrations in the system partition function.

5 Conclusions

In this work, we implemented the nested sampling (NS) algorithm for surfaces and extended its application to predict coverage-temperature surface phase diagrams. We demonstrated that NS enables the determination of surface thermodynamic properties at finite temperatures. We performed NS to construct partition functions for surfaces of the Lennard-Jones (LJ) solid having fixed and free particles. We further calculated the constant-volume heat capacity from the partition function, whose peaks were used to draw the coverage-temperature surface phase diagrams. By examining the structures recorded during the sampling and the order parameters calculated from these structures, we show that the free particles typically undergo two phase transitions, an enthalpy-driven condensation at a higher temperature and an entropy-driven reordering process at a lower temperature. This work sets the stage for the future implementation of surface NS for open thermodynamic systems and those with more than one chemical species, which carry great relevance in the search for the interfacial phases that govern materials performance for commercial and industrial applications and climate-change mitigation.

Acknowledgement

RBW acknowledges start-up funds from Washington University in St. Louis. LBP acknowledges support from the EPSRC through an individual Early Career Fellowship (EP/T000163/1). MY used resources from the Argonne Leadership Computing Facility, a DOE Office of Science User Facility supported under Contract DE-AC02-06CH11357. LBP used computing facil-

ties provided by the Scientific Computing Research Technology Platform of the University of Warwick.

Supporting Information Available

S1 Finite-Size Effects

We first examine how the calculated thermodynamic properties change on a smaller 2×2 per monolayer (ML) unit cell, where the finite-size effects should be more pronounced. Additionally, a smaller unit cell allows us to increase the number of free particles in the system to form more than one ML. The results are presented in Figure S1.

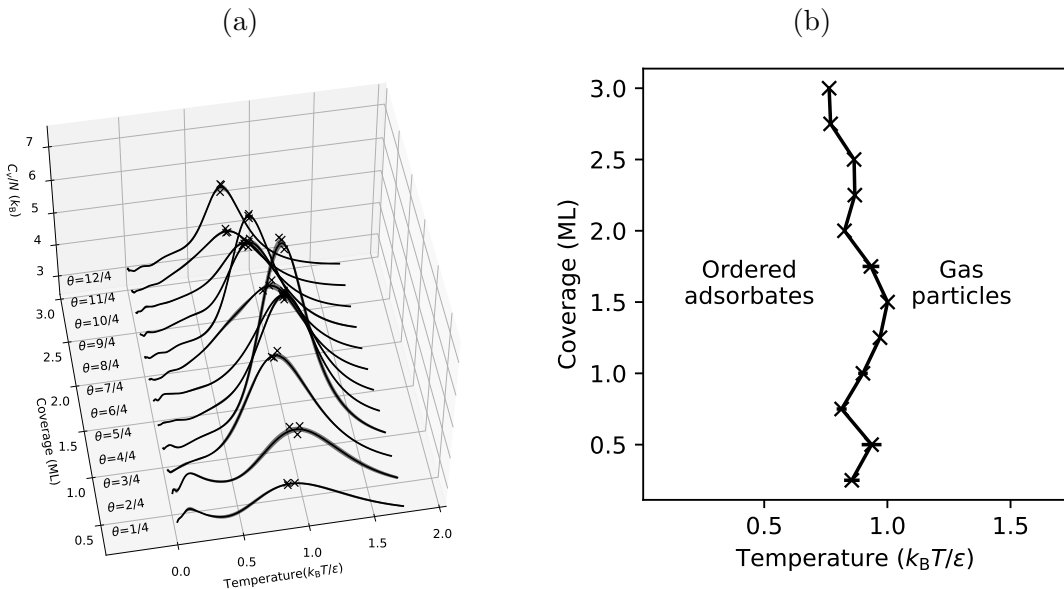


Figure S1: Calculated coverage-temperature properties of the flat LJ(111) surface with fractional coverages from $\theta = 1/4$ ML up to three MLs: (a) heat capacity per free particle, with the peaks on the curves marked with crosses (\times), and (b) phase diagram. The lines between the crosses are only guides for the eye.

One can see that the finite-size effect is significant. The lower-temperature entropy-induced peaks in the heat capacity curves are not found (besides the one- and two-free-particle cases $\theta = 1/4$ and $2/4$ ML), which is intuitive as the number of configurations on a 2×2 surface is significantly lower than the one with 4×4 surface particles. Nevertheless, the smaller system allows us to examine the phase transitions with surface coverages beyond one monolayer, where the transition temperatures exhibit weak coverage dependency.

S2 Additional Details on Surface System Setup

In this section, we compare the computational outputs from nested sampling (NS) with correct and incorrect system setups, illustrating the importance of having the appropriate configuration for the sampled system.

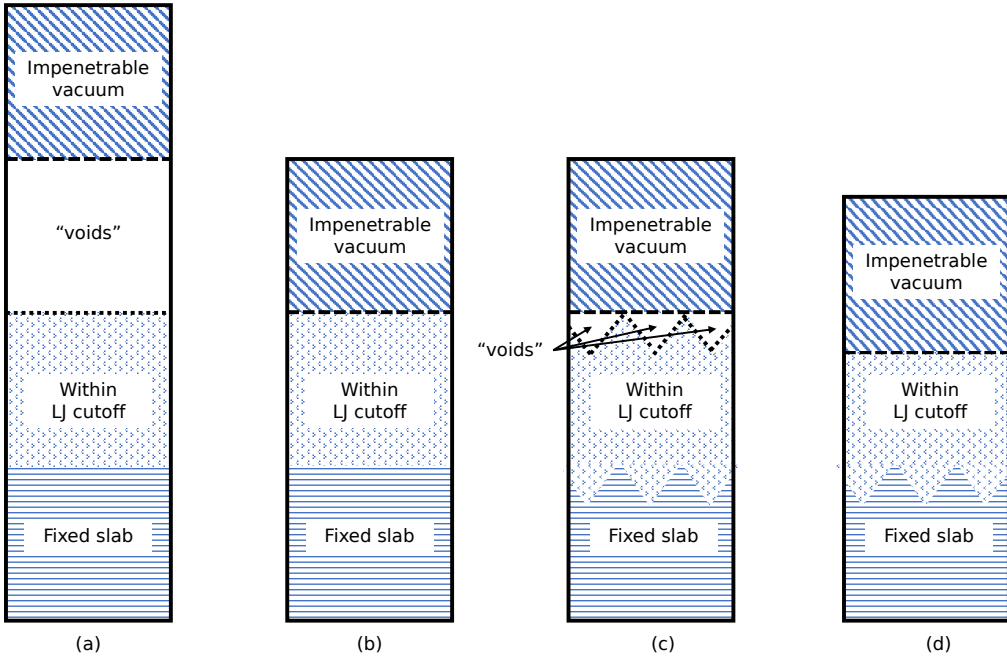


Figure S2: Different ways to construct the fixed surface–free particles model: The key is to ensure that all free particles can feel the surface. In setup (a), there is a large volume outside the Lennard-Jones cutoff, labeled as “voids”, where the free particles cannot interact with the fixed surface. Such a setup is considered problematic in this work, as we may accidentally sample the clustering of particles in the “voids”. Setup (b) is appropriate for flat surfaces. The “voids” are removed by reducing the overall height of the cell. Such a setup is used for LJ(111) and LJ(100) surfaces. However, even with reduced cell height, significant “voids” can still appear, as shown in (c), with stepped surfaces such as LJ(311) and LJ(110). We further reduced the cell’s height to correct it, as shown in (d).

To adequately capture the interplay between the free particles and the host surface, we want to ensure that the LJ interaction from the surface covers the entire volume of the available space. Otherwise, during the sampling, the particles can move into regions without interaction, causing either no energy contribution or incorrect contribution from particle-particle interactions instead of particle-surface interaction. Figure S2 shows several

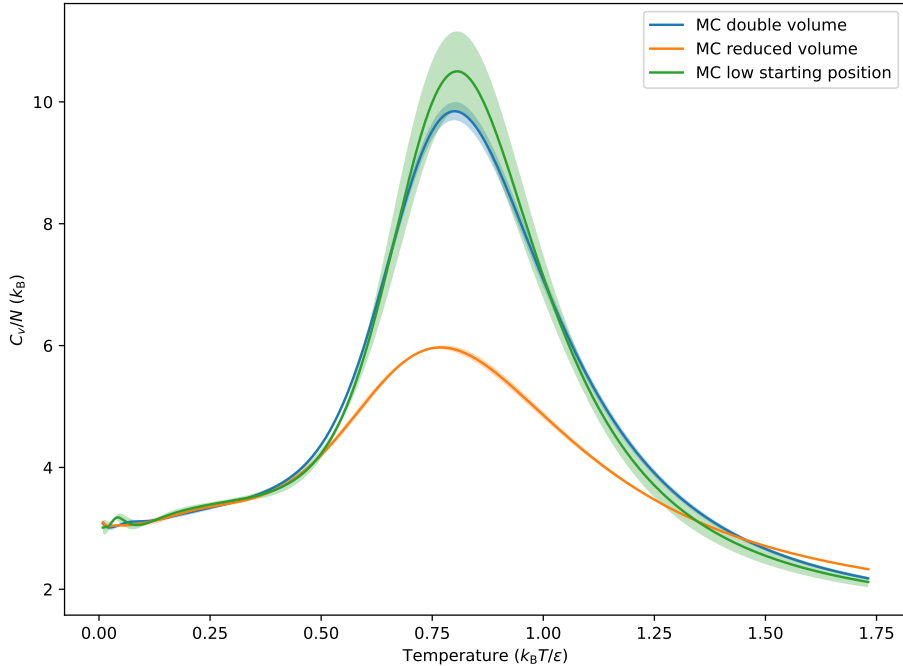


Figure S3: Heat capacity of a 2×2 LJ(111) surface with three free particles. The “double volume” (blue) curves are produced from NS with the setup shown in Figure S2(a). The “reduced volume” curves are from the setup shown as Figure S2(b). The “low starting positions” (green) curves are generated by using the setup in Figure S2(a) but placing all initial walkers within the LJ cutoff range, where the overall volume is the same. Still, all free particles can interact with the surface initially. Only the “reduced volume” (orange) curves are considered for this study.

scenarios of system setup that lead to different final results.

We have conducted tests on how the presence of “voids” and the placement of initial walkers influence the NS process and the calculated heat capacities. Three tests were carried out on a 2×2 LJ(111) surface with three free particles. The results are summarized in Figure S3. The first set of tests used the “double volume” setup as shown in Figure S2(a). The second set of tests used the “reduced volume” setup as shown in Figure S2(b). The third set of testings used the setup as shown in Figure S2(a) but placing all initial walkers within the LJ cutoff range (labeled as “low starting positions” in Figure S3), where the overall volume is the same but all free particles can interact with the surface initially. However, such a setup does not fulfill the requirement of having a uniform distribution of initial walkers in the configurational space. We can see that the overall volume determines the

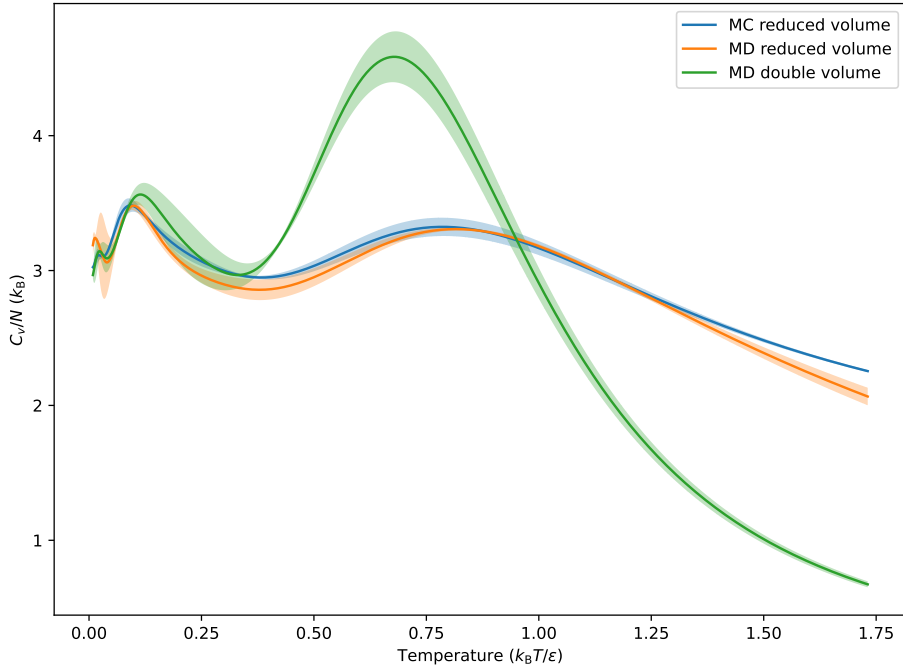


Figure S4: Heat capacity of a 2×2 LJ(111) surface with a single free particle. “MD” in the legend indicates that the free particle is propagated with the molecular dynamics (MD) in LAMMPS. The NS runs with the “double volume” setup as shown in Figure S2(a) get stuck whenever the single particle is in a “void.” The “reduced volume” (blue) curves are from setup as shown in Figure S2(b), which are the correct results, verified by the MD (orange) results using LAMMPS with the identical system setup.

height (hence the sharpness) of the peak in the C_V curves and influences the transition temperature slightly. This volume dependence is not surprising as the difference in volume leads to changes in other conditions, *e.g.* pressure, thus changing the C_V . Interestingly, the “low starting positions” setup recovers the same C_V , although with significant variance, even though a non-uniform distribution of initial walkers is used. This work considers the setup used to produce the orange curves in Figure S3 appropriate.

Furthermore, we encountered a technical challenge when running NS for any surfaces with a single free particle when using the “double volume” setup as shown in Figure S2(a). The sampling can stall when the free particle is placed in the “void” region, either by a Monte Carlo (MC) move or generated as an initial walker. As the “void” region is rather large and there are no other particles to interact with, it is challenging to generate a new

configuration with lower energy with random MC moves (due to the small step size relative to the cell’s dimensions). NS with MD can proceed with the “double volume” setup (green curves in Figure S4) through the `nve` propagation. As discussed above, the phase transitions, especially the higher-temperature condensation process, significantly change with the additional volume. We prefer eliminating the additional vacuum outside the LJ cutoff range to produce consistent C_V with only Monte-Carlo propagation.

S3 Surface Structures

In Table S1, we report the parameters of the four facets of the LJ solid. The cell dimensions are the dimensions of the simulation cell used in the NS calculations. The vacuum thickness is the distance between the topmost fixed layers and the reflective wall (at 4σ below the top of the simulation cell), and the thickness is less than or equal to the LJ potential cutoff. The slab thickness is the distance between the topmost fixed layers and the bottom of the cell. For each facet, there are different numbers of layers depending on the inter-layer spacing. The trough spacing is the distance between the centers of two neighboring troughs [for the (110) and (311) facets].

Table S1: The parameters of the four facets of the LJ solid, all in units of σ : cell dimensions ($x \times y \times z$); The vacuum thickness is the distance between the topmost fixed layers and the reflective wall; The slab thickness is the distance between the topmost fixed layers and the bottom of the cell; The number of layers within the fixed slab; The inter-layer spacing is the distance between two layers in the fixed slab; The troughs spacing is the distance between the centers of two neighboring troughs.

Facet	Cell dimensions	Vacuum thickness	Slab thickness	Number of layers	Inter-layer spacing	Trough spacing
(111)	$4.49 \times 3.89 \times 11.66$	4.00	3.66	5	0.92	—
(110)	$6.34 \times 4.49 \times 11.37$	3.44	3.93	8	0.56	1.60
(100)	$4.49 \times 4.49 \times 11.97$	4.00	3.97	6	0.79	—
(311)	$4.49 \times 7.44 \times 11.35$	3.52	3.83	9	0.48	1.86

S4 Phase Diagrams for Flat LJ(100) and Stepped LJ(110) Surfaces

As the LJ(100) and LJ(111) surfaces share similarities in terms of their surface features and phase behaviors, we only present the LJ(111) results in the main text. Most of the phase behaviors of the LJ(100) surface can be understood following the discussions of the LJ(111) surface. Here, we only highlight specific differences between the two surfaces. Compared to LJ(111), LJ(100) is also considered a flat surface but with reduced surface symmetry (four-fold *vs.* six-fold). This reduction leads to broader and lower low-temperature peaks in the C_V curves (Figure S5a) for coverages $\theta \leq 10/16$ ML. For $\theta > 10/16$ ML, the low- T peaks disappear. We manually determine a “shoulder” peak for each C_V curve with $\theta > 10/16$ ML and mark them with ♦ in Figure S5. One can see that heat capacity peaks for the entropy-driven ordering phase transition are being diminished as coverage increases beyond the half-ML ($\theta = 8/16$ ML), where the coordination number is being maximized. Note that the maximum coordination number for surface particles in a (100) ML is eight, with four from the slab and four from neighboring particles. It is interesting to see that the triple point is absent in the LJ(100) phase diagram (Figure S5b), which is present in the LJ(111) phase diagram. This absence indicates that, on LJ(111), for high surface coverages, the entropic and enthalpic effects compete, whereas, on LJ(100), the entropy-driven (lower temperature) ordering phase transition disappears while the enthalpy-driven (higher temperature) condensation phase transition remains unaffected.

S4.1 Stepped LJ(311) Surface

The stepped surface with a higher Miller index has surface features such as “troughs” along one of the lateral directions, offering several different binding sites compared to the flat LJ(111) facet. The potential energy landscape of LJ(311) is more complex than LJ(111), and its surface phase diagram is more difficult to determine. We compute the $C_V(T)$ for the LJ(311) surface with the same coverages as those for the flat LJ(111) surface. The $C_V(T)$

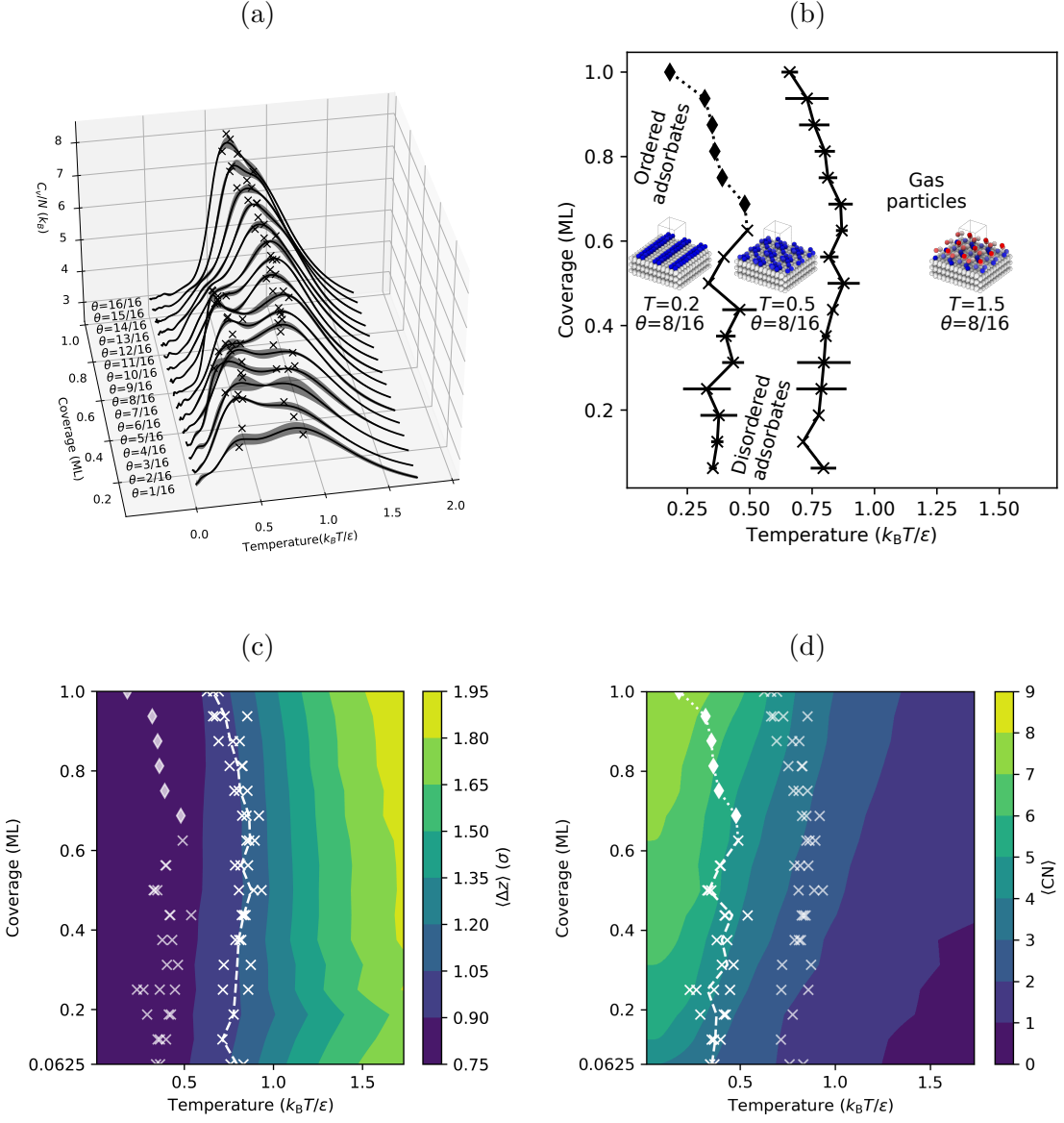


Figure S5: Calculated coverage-temperature properties of the flat LJ(100) surface with fractional coverages from $\theta = 1/16$ up to one ML: (a) heat capacity per free particle, with the peaks on the curves marked with crosses (\times), (b) phase diagram with insets showing the maximum-probability structures of each phase at selected temperatures for $\theta = 8/16$, (c) average z -coordinates of the free particles relative to the topmost layer in the fixed slab, note that in an LJ(100) bulk the interlayer spacing is 0.79σ , and (d) average coordination numbers of the free particles including both particle-particle and particle-surface bonding. The lines between the crosses are only guides for the eye. The diamond markers (\blacklozenge) indicate the disappearing peaks not found by the automated procedure.

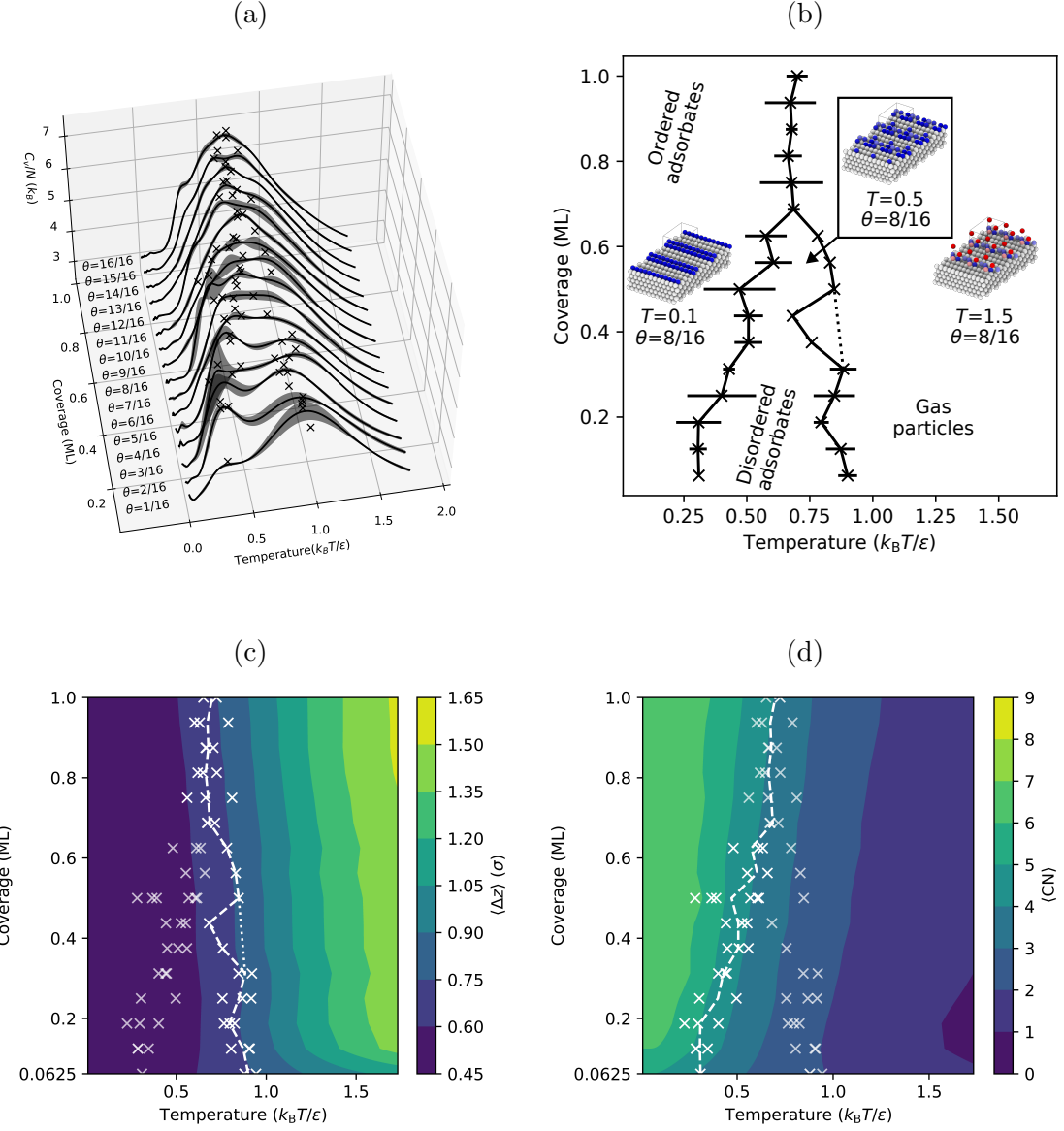


Figure S6: Calculated coverage-temperature properties of the flat LJ(311) surface with fractional coverages from $\theta = 1/16$ ML up to one ML: (a) heat capacity per free particle, with the peaks on the curves marked with crosses (×), (b) phase diagram with insets showing the maximum-probability structures of each phase at selected temperatures for $\theta = 8/16$ ML, (c) average z -coordinates of the free particles relative to the topmost layer in the fixed slab, note that for LJ(311), the interlayer spacing is 0.48σ , and (d) average coordination numbers of the free particles including both particle-particle and particle-surface bonding. The lines between the crosses are only guides for the eye.

curves are shown in Figure S6a. The $C_V(T)$ curves for the LJ(311) surface are more difficult to interpret than those for the LJ(111) surface. Firstly, the LJ(311) $C_V(T)$ curves from the NS runs show larger deviations near the peaks than those for LJ(111). Moreover, the peaks are generally much broader and overlap significantly, making them more difficult to determine precisely. For example, at $\theta = 6/16$ and $7/16$, the C_V curves have a plateau-like feature from $T = 0.5 - 0.8 k_B T/\epsilon$. Nevertheless, we employed the same automated procedure to find the peaks. Despite the larger deviations, it is clear to see that for each of the lower coverages ($\theta \leq 10$), there are two separate peaks: one at a higher temperature between 0.7 and $0.9 k_B T/\epsilon$ (see \times s), and another peak at a lower temperature between 0.2 and $0.6 k_B T/\epsilon$. Compared to the C_V curves of LJ(111), the low-coverage high-temperature peaks of LJ(311) are more dominant. For higher coverages ($\theta \geq 11/16$), the two peaks on the C_V curves merged into one, similar to the behavior previously observed on LJ(111) at higher coverages. The merged peaks are mostly located at a temperature between 0.6 and $0.8 k_B T/\epsilon$ and are much broader and lower than those for LJ(111).

We further project the temperatures of all peaks onto the coverage-temperature plot to construct the phase diagram for LJ(311), as shown in Figure S6b. Due to the more significant deviations of the peak temperatures from the C_V curves, the phase boundaries are less clearly defined comparing to those for LJ(111). That said, the overall features of the LJ(311) phase diagram are still qualitatively similar to LJ(111): two phase transitions for coverages $\theta \leq 10$, a triple point located at $T \approx 0.7 k_B T/\epsilon$ and $\theta = 11/16$, and a single phase transition for coverages $\theta \geq 12/16$. Note that, due to the flatness of the C_V curves at $\theta = 6/16$ and $7/16$, the peaks found by the `scipy.signal.find_peaks()` function may not be reliable. Therefore, we join high-temperature peaks at $\theta = 5/16$ and $8/16$, marked by the dotted line in Figure S6b, to show a more likely phase boundary.

In order to further understand the phase transitions on the LJ(311) surface, we also compute surface order parameters, including $\langle \Delta z \rangle$ (Figure S6c) and $\langle \text{CN} \rangle$ (Figure S6d). We can also utilize the results from LJ(111) and LJ(110) to intuit the phase transitions on the

LJ(311) surface. The LJ(311) can be understood as an in-between surface from a completely flat LJ(111) to the stepped LJ(110). The troughs on LJ(311) are shallower than LJ(110), and the inter-through spacing is larger (see Table S1), hence is more “flat”.

S5 Maximum-Probability Structures

We include top and side views of all four different facets at selected temperatures at all coverages as separate files:

- LJ(111) surface: 111-4x4-grid-top.png and 111-4x4-grid-side.png
- LJ(311) surface: 311-4x4-grid-top.png and 311-4x4-grid-side.png
- LJ(100) surface: 100-4x4-grid-top.png and 100-4x4-grid-side.png
- LJ(110) surface: 110-4x4-grid-top.png and 110-4x4-grid-side.png

References

- (1) Wander, A.; Schedin, F.; Steadman, P.; Norris, A.; McGrath, R.; Turner, T. S.; Thornton, G.; Harrison, N. M. Stability of Polar Oxide Surfaces. *Phys. Rev. Lett.* **2001**, *86*, 3811–3814.
- (2) Ravi, V. K.; Santra, P. K.; Joshi, N.; Chugh, J.; Singh, S. K.; Rensmo, H.; Ghosh, P.; Nag, A. Origin of the Substitution Mechanism for the Binding of Organic Ligands on the Surface of CsPbBr_3 Perovskite Nanocubes. *J. Phys. Chem. Lett.* **2017**, *8*, 4988–4994.
- (3) Ohmann, R.; Ono, L. K.; Kim, H.-S.; Lin, H.; Lee, M. V.; Li, Y.; Park, N.-G.; Qi, Y. Real-Space Imaging of the Atomic Structure of Organic–Inorganic Perovskite. *J. Am. Chem. Soc.* **2015**, *137*, 16049–16054.
- (4) Chen, Z.; Martirez, J. M. P.; Zahl, P.; Carter, E. A.; Koel, B. E. Self-assembling of formic acid on the partially oxidized p (2×1) $\text{Cu}(110)$ surface reconstruction at low coverages. *J. Chem. Phys.* **2019**, *150*, 041720.
- (5) Phan, T. H.; Banjac, K.; Cometto, F. P.; Dattila, F.; García-Muelas, R.; Raaijeman, S. J.; Ye, C.; Koper, M. T. M.; López, N.; Lingenfelder, M. Emergence of Potential-Controlled Cu-Nanocuboids and Graphene-Covered Cu-Nanocuboids under *Operando* CO_2 Electroreduction. *Nano Lett.* **2021**, *21*, 2059–2065.
- (6) Cheng, D.; Wei, Z.; Zhang, Z.; Broekmann, P.; Alexandrova, A. N.; Sautet, P. Restructuring and Activation of $\text{Cu}(111)$ under Electrocatalytic Reduction Conditions. *Angewandte Chemie* **2023**, *135*, e202218575.
- (7) Wan, C.; Zhang, Z.; Dong, J.; Xu, M.; Pu, H.; Baumann, D.; Lin, Z.; Wang, S.; Huang, J.; Shah, A. H.; Pan, X.; Hu, T.; Alexandrova, A. N.; Huang, Y.; Duan, X. Amorphous nickel hydroxide shell tailors local chemical environment on platinum surface for alkaline hydrogen evolution reaction. *Nat. Mater.* **2023**,

- (8) Zhang, Z.; Wei, Z.; Sautet, P.; Alexandrova, A. N. Hydrogen-Induced Restructuring of a Cu(100) Electrode in Electroreduction Conditions. *J. Am. Chem. Soc.* **2022**, *144*, 19284–19293.
- (9) Martirez, J. M. P.; Kim, S.; Morales, E. H.; Diroll, B. T.; Cargnello, M.; Gordon, T. R.; Murray, C. B.; Bonnell, D. A.; Rappe, A. M. Synergistic Oxygen Evolving Activity of a TiO₂-Rich Reconstructed SrTiO₃ (001) Surface. *J. Am. Chem. Soc.* **2015**, *137*, 2939–2947.
- (10) Weber, M. L.; Lole, G.; Kormanyos, A.; Schwiers, A.; Heymann, L.; Speck, F. D.; Meyer, T.; Dittmann, R.; Cherevko, S.; Jooss, C.; Baeumer, C.; Gunkel, F. Atomistic Insights into Activation and Degradation of La_{0.6}Sr_{0.4}CoO_{3-δ} Electrocatalysts under Oxygen Evolution Conditions. *J. Am. Chem. Soc.* **2022**, *144*, 17966–17979.
- (11) Akbashev, A. R.; Roddatis, V.; Baeumer, C.; Liu, T.; Mefford, J. T.; Chueh, W. C. Probing the stability of SrIrO₃ during active water electrolysis *via operando* atomic force microscopy. *Energy Environ. Sci.* **2023**, *16*, 513–522.
- (12) Schröder, J.; Zamora Zeledón, J. A.; Kamat, G. A.; Kreider, M. E.; Wei, L.; Mule, A. S.; Torres, A.; Yap, K.; Sokaras, D.; Gallo, A.; Stevens, M. B.; Jaramillo, T. F. Tracking the Dynamics of a Ag-MnO_x Oxygen Reduction Catalyst Using In Situ and Operando X-ray Absorption Near-Edge Spectroscopy. *ACS Energy Lett.* **2023**, 2962–2969.
- (13) Akbashev, A. R. Electrocatalysis on oxide surfaces: Fundamental challenges and opportunities. *Current Opinion in Electrochemistry* **2022**, *35*, 101095.
- (14) Grumelli, D.; Wiegmann, T.; Barja, S.; Reikowski, F.; Maroun, F.; Allongue, P.; Balajka, J.; Parkinson, G. S.; Diebold, U.; Kern, K.; Magnussen, O. M. Electrochemical Stability of the Reconstructed Fe₃O₄ (001) Surface. *Angew. Chem. Int. Ed.* **2020**, *59*, 21904–21908.

- (15) Reuter, K.; Scheffler, M. Composition, structure, and stability of RuO₂(110) as a function of oxygen pressure. *Phys. Rev. B* **2001**, *65*, 035406.
- (16) Zhou, Y.; Scheffler, M.; Ghiringhelli, L. M. Determining surface phase diagrams including anharmonic effects. *Phys. Rev. B* **2019**, *100*, 174106.
- (17) Ulissi, Z. W.; Singh, A. R.; Tsai, C.; Nørskov, J. K. Automated Discovery and Construction of Surface Phase Diagrams Using Machine Learning. *J. Phys. Chem. Lett.* **2016**, *7*, 3931–3935.
- (18) Schusteritsch, G.; Pickard, C. J. Predicting interface structures: From SrTiO₃ to graphene. *Phys. Rev. B* **2014**, *90*, 035424.
- (19) Timmermann, J.; Kraushofer, F.; Resch, N.; Li, P.; Wang, Y.; Mao, Z.; Riva, M.; Lee, Y.; Staacke, C.; Schmid, M.; Scheurer, C.; Parkinson, G. S.; Diebold, U.; Reuter, K. IrO₂ Surface Complexions Identified through Machine Learning and Surface Investigations. *Phys. Rev. Lett.* **2020**, *125*, 206101.
- (20) Rønne, N.; Christiansen, M.-P. V.; Slavensky, A. M.; Tang, Z.; Brix, F.; Pedersen, M. E.; Bisbo, M. K.; Hammer, B. Atomistic structure search using local surrogate model. *J. Chem. Phys.* **2022**, *157*, 174115.
- (21) Sun, G.; Fuller, J. T.; Alexandrova, A. N.; Sautet, P. Global Activity Search Uncovers Reaction Induced Concomitant Catalyst Restructuring for Alkane Dissociation on Model Pt Catalysts. *ACS Catal.* **2021**, *11*, 1877–1885.
- (22) Chen, D.; Shang, C.; Liu, Z.-P. Automated search for optimal surface phases (ASOPs) in grand canonical ensemble powered by machine learning. *J. Chem. Phys.* **2022**, *156*, 094104.
- (23) Zhu, Q.; Li, L.; Oganov, A. R.; Allen, P. B. Evolutionary method for predicting surface reconstructions with variable stoichiometry. *Phys. Rev. B* **2013**, *87*, 195317.

- (24) Chiriki, S.; Christiansen, M.-P. V.; Hammer, B. Constructing convex energy landscapes for atomistic structure optimization. *Phys. Rev. B* **2019**, *100*, 235436.
- (25) Wang, Y.; Su, Y.-Q.; Hensen, E. J. M.; Vlachos, D. G. Finite-Temperature Structures of Supported Subnanometer Catalysts Inferred *via* Statistical Learning and Genetic Algorithm-Based Optimization. *ACS Nano* **2020**, *14*, 13995–14007.
- (26) Wanzenböck, R.; Arrigoni, M.; Bichelmaier, S.; Buchner, F.; Carrete, J.; Madsen, G. K. H. Neural-network-backed evolutionary search for SrTiO₃ (110) surface reconstructions. *Digital Discovery* **2022**, *1*, 703–710.
- (27) Lu, S.; Wang, Y.; Liu, H.; Miao, M.-s.; Ma, Y. Self-assembled ultrathin nanotubes on diamond (100) surface. *Nat Commun* **2014**, *5*, 3666.
- (28) Bisbo, M. K.; Hammer, B. Efficient Global Structure Optimization with a Machine-Learned Surrogate Model. *Phys. Rev. Lett.* **2020**, *124*, 086102.
- (29) Jørgensen, M. S.; Mortensen, H. L.; Meldgaard, S. A.; Kolsbjerg, E. L.; Jacobsen, T. L.; Sørensen, K. H.; Hammer, B. Atomistic structure learning. *The Journal of Chemical Physics* **2019**, *151*, 054111.
- (30) Zhang, Z.; Zandkarimi, B.; Alexandrova, A. N. Ensembles of Metastable States Govern Heterogeneous Catalysis on Dynamic Interfaces. *Acc. Chem. Res.* **2020**, *53*, 447–458.
- (31) Fantauzzi, D.; Krick Calderón, S.; Mueller, J. E.; Grabau, M.; Papp, C.; Steinrück, H.-P.; Senftle, T. P.; van Duin, A. C. T.; Jacob, T. Growth of Stable Surface Oxides on Pt(111) at Near-Ambient Pressures. *Angew. Chem. Int. Ed.* **2017**, *56*, 2594–2598.
- (32) Wexler, R. B.; Qiu, T.; Rappe, A. M. Automatic Prediction of Surface Phase Diagrams Using Ab Initio Grand Canonical Monte Carlo. *J. Phys. Chem. C* **2019**, *123*, 2321–2328.

- (33) Somjit, V.; Yildiz, B. Atomic and Electronic Structure of the Al₂O₃/Al Interface during Oxide Propagation Probed by Ab Initio Grand Canonical Monte Carlo. *ACS Appl. Mater. Interfaces* **2022**, *14*, 42613–42627.
- (34) Xu, J.; Xie, W.; Han, Y.; Hu, P. Atomistic Insights into the Oxidation of Flat and Stepped Platinum Surfaces Using Large-Scale Machine Learning Potential-Based Grand-Canonical Monte Carlo. *ACS Catal.* **2022**, *12*, 14812–14824.
- (35) Du, X.; Damewood, J. K.; Lunger, J. R.; Millan, R.; Yildiz, B.; Li, L.; Gómez-Bombarelli, R. Machine-learning-accelerated simulations enable heuristic-free surface reconstruction. 2023; <http://arxiv.org/abs/2305.07251>.
- (36) Skilling, J. Nested Sampling. Bayesian Inference and Maximum Entropy Methods in Science and Engineering: 24th International Workshop on Bayesian Inference and Maximum Entropy Methods in Science and Engineering. 2004; pp 395–405.
- (37) Skilling, J. Nested sampling for general Bayesian computation. *Bayesian Analysis* **2006**, *1*, 833–859.
- (38) Ashton, G.; Bernstein, N.; Buchner, J.; Chen, X.; Csányi, G.; Fowlie, A.; Feroz, F.; Griffiths, M.; Handley, W.; Habeck, M.; Higson, E.; Hobson, M.; Lasenby, A.; Parkinson, D.; Pártay, L. B.; Pitkin, M.; Schneider, D.; Speagle, J. S.; South, L.; Veitch, J.; Wacker, P.; Wales, D. J.; Yallup, D. Nested sampling for physical scientists. *Nat Rev Methods Primers* **2022**, *2*, 39.
- (39) Pártay, L. B.; Bartók, A. P.; Csányi, G. Efficient Sampling of Atomic Configurational Spaces. *J. Phys. Chem. B* **2010**, *114*, 10502–10512.
- (40) Baldock, R. J. N.; Pártay, L. B.; Bartók, A. P.; Payne, M. C.; Csányi, G. Determining pressure-temperature phase diagrams of materials. *Phys. Rev. B* **2016**, *93*, 174108.

- (41) Pártay, L. B.; Csányi, G.; Bernstein, N. Nested sampling for materials. *Eur. Phys. J. B* **2021**, *94*, 159.
- (42) Rossi, K.; Pártay, L. B.; Csányi, G.; Baletto, F. Thermodynamics of CuPt nanoalloys. *Sci Rep* **2018**, *8*, 9150.
- (43) Dorrell, J.; B. Pártay, L. Thermodynamics and the potential energy landscape: case study of small water clusters. *Phys. Chem. Chem. Phys.* **2019**, *21*, 7305–7312.
- (44) Szekeres, B.; Pártay, L. B.; Mátyus, E. Direct Computation of the Quantum Partition Function by Path-Integral Nested Sampling. *J. Chem. Theory Comput.* **2018**, *14*, 4353–4359.
- (45) Bolhuis, P. G.; Csányi, G. Nested Transition Path Sampling. *Phys. Rev. Lett.* **2018**, *120*, 250601.
- (46) Baldock, R. J. N.; Bernstein, N.; Salerno, K. M.; Pártay, L. B.; Csányi, G. Constant-pressure nested sampling with atomistic dynamics. *Phys. Rev. E* **2017**, *96*, 043311.
- (47) Gola, A.; Pastewka, L. Embedded atom method potential for studying mechanical properties of binary Cu–Au alloys. *Modelling Simul. Mater. Sci. Eng.* **2018**, *26*, 055006.
- (48) Dorrell, J.; Pártay, L. B. Pressure–Temperature Phase Diagram of Lithium, Predicted by Embedded Atom Model Potentials. *J. Phys. Chem. B* **2020**, *124*, 6015–6023.
- (49) Bartók, A. P.; Hantal, G.; Pártay, L. B. Insight into Liquid Polymorphism from the Complex Phase Behavior of a Simple Model. *Phys. Rev. Lett.* **2021**, *127*, 015701.
- (50) Martiniani, S.; Stevenson, J. D.; Wales, D. J.; Frenkel, D. Superposition Enhanced Nested Sampling. *Phys. Rev. X* **2014**, *4*, 031034.
- (51) Tran, R.; Xu, Z.; Radhakrishnan, B.; Winston, D.; Sun, W.; Persson, K. A.; Ong, S. P. Surface energies of elemental crystals. *Sci. Data* **2016**, *3*, 160080.

- (52) Pártay, L. B.; Ortner, C.; Bartók, A. P.; Pickard, C. J.; Csányi, G. Polytypism in the ground state structure of the Lennard-Jonesium. *Phys. Chem. Chem. Phys.* **2017**, *19*, 19369–19376.
- (53) Somasi, S.; Khomami, B.; Lovett, R. Computer simulation of surface and adatom properties of Lennard-Jones solids: A comparison between face-centered-cubic and hexagonal-close-packed structures. *The Journal of Chemical Physics* **2001**, *114*, 6315–6326.
- (54) Rosenbrock, C. W.; Gubaev, K.; Shapeev, A. V.; Pártay, L. B.; Bernstein, N.; Csányi, G.; Hart, G. L. W. Machine-learned interatomic potentials for alloys and alloy phase diagrams. *npj Comput Mater* **2021**, *7*, 24.

TOC Graphic

